ACS APPLIED NANO MATERIALS

www.acsanm.org
Article

Efficient Lasing in MoS_2/WSe_2-Based Metasurfaces Enabled by Quasi-Dark Magnetic Dipole Resonance

Georgios Nousios,* Thomas Christopoulos, Emmanouil E. Kriezis, and Odysseas Tsilipakos*

Cite This: *ACS Appl. Nano Mater.* 2026, 9, 2301−2308
Read Online

ABSTRACT: The combination of a strongly resonant optical metasurface (MS) with a MoS_2/WSe_2 heterobilayer is proposed for efficient free-space lasing enabled by the enhanced coupling between the optical and matter (exciton) states. The MS comprises silicon-rich nitride meta-atoms periodically arrayed in a subdiffractive lattice and overlaid with MoS_2/WSe_2, which provides an optically pumped gain around 1130 nm. Light emission is enabled by exploiting a quasi-bound state in the continuum in the form of a perturbed vertical magnetic dipole resonance. Following a meticulous design process guided by full-wave simulations and multipole expansion analysis, an ultralow lasing threshold of ∼6 kW/cm^2 is achieved. Moreover, the thermal stability of the lasing structure is examined through heat-transfer simulations; stable operation with pump power densities up to a few MW/cm^2 (3 orders of magnitude above the threshold) is predicted. These results demonstrate that MoS_2/WSe_2-based MS lasers can exhibit robust operation, paving the way for highly performing ultrathin light-emitting surfaces. The lasing response is rigorously assessed through a highly efficient temporal coupled-mode theory framework, verified by time-domain FEM simulations showing excellent agreement. Thus, an efficient and accurate approach to design and study MS lasers with arbitrary geometries and surface or bulk gain media is introduced, exhibiting significant advantages over cumbersome full-wave simulations.

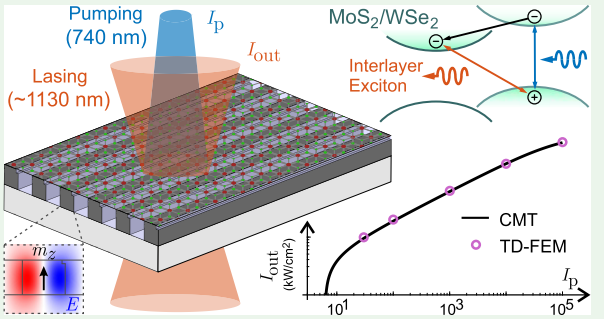

KEYWORDS: *light-emitting metasurfaces, bound states in the continuum, transition-metal dichalcogenides, two-dimensional materials, temporal coupled-mode theory*

1. INTRODUCTION

Light-emitting surfaces, where a strongly resonant metasurface (MS) acts as the optical cavity, have concentrated significant attention during the past decade.[1,2] In particular, dielectric optical MSs supporting bound states in the continuum (BICs) offer an attractive route to achieving efficient ultrathin lasing elements with tunable emission properties.[1,3] Being decoupled from radiation fields, BICs are characterized by theoretically infinite radiative quality factors; their total quality factor (Q) is limited only by material absorption and fabrication imperfections. In practical light-emitting MSs, radiation leakage has to be allowed in order to outcouple the emitted light.[4] To this end, BICs are transformed into quasi-BICs (qBICs) with finite, yet very high, radiative quality factors. In the most common case of symmetry-protected BICs, this transformation can be performed controllably by introducing structural asymmetries in the MS unit cell.[4−7] Thus, a number of MS lasers have been recently proposed and realized, exploiting a range of different symmetry-protected BIC resonances. These include vertical electric,[8] magnetic,[9] and toroidal[10] dipoles, as well as higher-order dark Mie multipoles, such as electric octupoles,[11] and dark surface lattice resonances.[12]

Alongside a strongly resonant optical state, an efficient and robust gain medium is required. The advent of two-dimensional (2D) direct-bandgap semiconductors, such as transition-metal dichalcogenides (TMDs),[13,14] has opened new prospects due to their extraordinary luminescence properties.[15,16] Recently, lasing MSs where the gain is provided by TMD *monolayers* have been proposed and realized.[11,17] Even more promising are TMD *heterobilayers* forming type-II band alignment heterostructures that host bright interlayer excitons.[18] The latter are characterized by long metastable lifetime exceeding 1 ns[19] (in stark contrast to the picosecond lifetimes of intralayer excitons[19,20]), high quantum yield, and electrically tunable luminescence properties in the near-infrared (NIR).[21]

One of the most promising bilayers is MoS_2/WSe_2 that emits in the range of 1100−1300 nm. It has been utilized in

Received: October 25, 2025
Revised: January 10, 2026
Accepted: January 15, 2026
Published: January 26, 2026

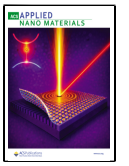

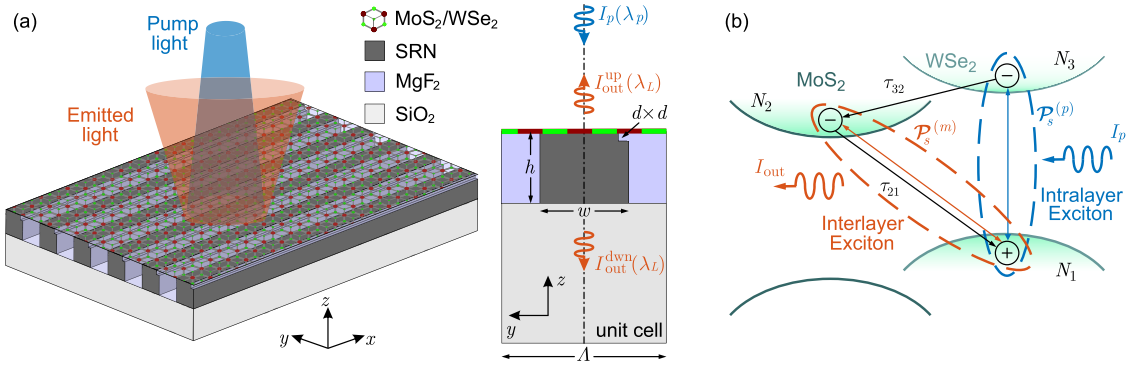

Figure 1. (a) Illustration of the considered MS laser consisting of symmetry-broken SRN stripes periodically arrayed on a SiO_2 substrate. The structure is planarized with a low-index cladding and is overlaid with the MoS_2/WSe_2 heterobilayer. The MS laser is optically pumped by a normally incident plane wave at λ_p and emits vertically in both $\pm\hat{z}$ directions at λ_L. The geometric parameters are annotated in the unit cell cross-section (right part). (b) Energy diagram of MoS_2/WSe_2 showing the lasing process due to the radiative recombination of interlayer excitons.

integrated nanophotonic light sources;[22−24] however, thus far, it has not been leveraged for light-emitting MSs. In this work, we investigate whether the combination of MoS_2/WSe_2 with a strongly resonant qBIC MS can enable efficient free-space lasing and allow for robust and stable operation. Specifically, we propose and theoretically study a dielectric MS laser composed of silicon-rich nitride (SRN) meta-atoms arrayed in a subdiffractive lattice and residing on a SiO_2 substrate. The MS is overlaid with MoS_2/WSe_2, which providesgain around 1130 nm after being optically pumped at 740 nm. Lasing is enabled by a vertical magnetic dipole mode supported by the MS, i.e., a symmetry-protected BIC.[25] The optical properties of the magnetic dipole qBIC are thoroughly studied through eigenfrequency finite element method (FEM) simulations and multipolar expansion analysis.[26] Upon appropriately breaking the symmetry, the emitted light is radiated in the normal direction by a large coherent aperture. The proposed MS laser is characterized by a low lasing threshold of ∼6 kW/cm^2, enabled by the enhanced coupling between the optical and matter (exciton) states, and an efficiency of ∼3.7%. Heat-transfer simulations indicate that the proposed laser can stably operate for pump irradiances up to a few MW/cm^2 (3 orders of magnitude above the threshold) unhindered by deleterious thermal effects. Therefore, our results demonstrate that MoS_2/WSe_2-based MS lasers can exhibit efficient and robust operation, suitable for practical applications. To assess the lasing response, we utilize a highly efficient temporal coupled-mode theory (CMT) framework for nanophotonic lasers, rigorously implementing a semiclassical description of the light−matter interactions at the nanoscale.[27,28] The CMT results are systematically verified against full-wave nonlinear time-domain FEM (TD-FEM) simulations, showing excellent agreement. Thus, another important contribution of this work is the introduction of an efficient and accurate approach to design and study MS lasers with arbitrary geometries and surface or bulk gain media without relying on cumbersome full-wave simulations.

The rest of the paper is organized as follows: In Section 2.1, the passive qBIC MS is designed, while in Section 2.2, the lasing response is thoroughly assessed. Section 2.3 addresses the thermal stability of the proposed lasing element, and Section 3 offers concluding remarks.

2. RESULTS AND DISCUSSION

2.1. Design of the Quasi-Dark MS

The MS under study is schematically depicted in Figure 1a. SRN stripes are periodically arrayed in a subdiffractive lattice of pitch Λ = 500 nm. We opt for the ultra-silicon-rich SRN compound of ref 29, characterized by a comparably high refractive index to silicon and an extended transparency window down to 605 nm. Taking advantage of the low dispersion of SRN in the NIR, we assume a wavelength-independent index of $n_{SRN} \approx 3.15$. The height of the SRN stripes is set to the typical value of h = 220 nm; their width is adjusted to w = 272 nm for the resonance wavelength of the lasing mode, i.e., the out-of-plane magnetic dipole, to fall near the maximum of the emission spectrum of MoS_2/WSe_2, i.e., 1128 nm (1.1 eV).[22] The MS resides on a SiO_2 substrate with n_{SiO_2} = 1.45. The structure is subdiffractive even in transmission for wavelengths $\lambda > n_{SiO_2}\Lambda$ = 725 nm under normal incidence. The periodic configuration is planarized with a MgF_2 cladding so that a flat surface is available for the TMD heterobilayer to reside on. MgF_2 is a favorable cladding material characterized by both a low refractive index n_{MgF_2} = 1.37 (resulting in strong index contrast with SRN) and high thermal conductivity (see Section 2.3). All the utilized dielectric materials are practically transparent at the wavelengths of interest and are considered lossless.

Among the dark Mie resonances supported by the dielectric MS, the out-of-plane magnetic dipole resonance (MD_z) is quite favorable for lasing applications involving gain provided by 2D semiconductors that reside atop the MS. This is because MD_z is characterized by an in-plane loop of polarization current, with the electric field being tangential and interacting strongly with the sheet material. On the contrary, out-of-plane electric and toroidal dipoles have a dominant vertical electric field component, rendering them ill-suited for enhanced light−matter interaction with 2D media. We focus on the TE (Transverse Electric) polarization, $\mathbf{E} = E_x\hat{\mathbf{x}}$, and examine the dark MD_z mode hosted by the examined passive structure (absence of MoS_2/WSe_2) via conducting eigenfrequency and plane-wave scattering simulations on the unit cell of the MS using COMSOL Multiphysics. The mode profile is depicted in the inset of Figure 2a, where color denotes Re$\{E_x\}$ and arrows indicate the magnetic field which lies exclusively on the yz plane. Since this is a 2D geometry, the polarization current

https://doi.org/10.1021/acsanm.5c04888
ACS Appl. Nano Mater. 2026, 9, 2301−2308

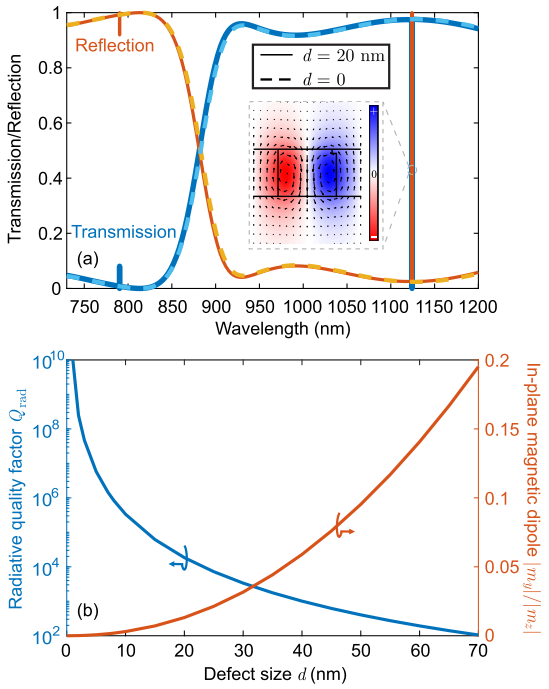

Figure 2. (a) Transmission and reflection spectra of the examined MS under vertical plane wave illumination when d = 20 nm (solid lines) and d = 0 nm (dashed lines). Inset: Field profile of the qBIC excited near ∼1128 nm when d = 20 nm. Color denotes Re$\{E_x\}$, whereas arrows indicate the magnetic field. (b) MD_z mode: radiative quality factor Q_{rad} and magnitude of the residual in-plane magnetic dipole moment m_y (normalized to the dominant vertical component) as a function of the defect size d.

loop that characterizes MD modes is not closed (Figure 2a); rather, it can be viewed as closing through infinity in the x direction.

When arrayed in a subdiffractive lattice, the MD_z mode constitutes a symmetry-protected BIC, which is completely decoupled from the radiation channel in the normal direction;[25] this is evident from the antisymmetric nature of the mode with respect to the xz center plane. Hence, a square sector with side d is removed from the upper right corner of the SRN stripes (Figure 1a), introducing the structural asymmetry (defect) that transforms the MD_z mode into a qBIC that can couple with free space. This is evident in Figure 2a, where the transmission and reflection spectra under vertical plane-wave illumination are presented for d = 0 and d = 20 nm. Only in the latter case, a sharp dip (peak) in transmission (reflection) emerges at the resonance wavelength of the MD_z mode, indicating that the qBIC mode can be excited. The structure also supports a magnetic quadrupole qBIC at ∼790 nm. We should note here that an actual MS would have a finite extent along the y axis. As shown in Section S1 of the Supporting Information (SI), even with 45 unit cells, the optical response under illumination by a loosely focused Gaussian beam is very similar to the ideal periodic structure (plane wave incidence).

The size d of the defect determines the radiative damping of MD_z. The radiative quality factor, Q_{rad}, of the mode as a function of d is presented in Figure 2b (blue line). When d = 0 (symmetric structure), Q_{rad} diverges to infinity; for $d \neq 0$, Q_{rad} becomes finite and can be tuned at will. Note that in practical realizations, the total Q is bounded by material losses and fabrication-related imperfections, as well as the finite size of the MS.[30] For lasing applications, values of the defect size d between 15 and 40 nm (corresponding to Q_{rad} values between ∼60,000 and 1000) attract the main interest as they can strike a compromise between achieving a high Q for low lasing threshold while permitting a sufficient amount of optical power to be emitted from the MS. The physical mechanism behind the transformation of the MD_z mode from BIC to qBIC can be revealed by conducting a multipole expansion on the polarization currents of the eigenvector, using the expressions of ref 26. When d = 0, the mode is solely characterized by the vertical magnetic dipole moment, m_z, while the other moments are zero. As d increases, the mode also acquires a small in-plane/tangential magnetic dipole moment m_y, which increases with d (red line in Figure 2b). In contrast to m_z, the m_y moment is bright meaning that it scatters in the normal $\pm\hat{\mathbf{z}}$ direction. Thus, the coupling of the MD_z mode with the radiation fields is mediated through the residual in-plane magnetic dipole moment that the mode acquires with the introduction of the defect.

2.2. Assesment of the Lasing Performance

We now proceed to assess the lasing performance of the qBIC MS overlaid with a MoS_2/WSe_2 heterostructure. The bilayer under study constitutes a three-level gain medium (Figure 1b). The pump wave excites the A intralayer excitons of WSe_2, with the intralayer excitonic (pump) transition being described by the induced surface electric polarization field $\mathcal{P}_s^{(p)}(\mathbf{r}, t)$. Subsequently, the photogenerated electrons transfer from the conduction band of WSe_2 to that of MoS_2 (type-II band alignment) with a characteristic carrier lifetime τ_{32}.[18] Consequently, interlayer excitons are formed, characterized by the overall recombination (radiative and nonradiative) carrier lifetime τ_{21}, for which we have $\tau_{21} \gg \tau_{32}$ resulting in the ability to attain population inversion between level 2 (conduction band of MoS_2) and level 1 (valence band of WSe_2). The interlayer excitonic (lasing) transition is described by a separate surface electric polarization field $\mathcal{P}_s^{(m)}(\mathbf{r}, t)$. Both of these fields follow Lorentzian oscillator equations:[24,31]

$$\frac{\partial^2 \mathcal{P}_s^{(k)}}{\partial t^2} + \Gamma_{iq}\frac{\partial \mathcal{P}_s^{(k)}}{\partial t} + \omega_{iq}^2 \mathcal{P}_s^{(k)} = -\sigma_{iq}\Delta N_{iq}\mathcal{E}_{\parallel} \tag{1}$$

where $k = \{p, m\}$, whereas $iq = \{31, 21\}$ denotes the levels of the gain medium related to each transition and $\Delta N_{iq}(\mathbf{r}, t) = N_i(\mathbf{r}, t) - N_q(\mathbf{r}, t)$ is the corresponding population inversion. Furthermore, ω_{iq} and Γ_{iq} are the central frequency and line width of each transition, respectively, while σ_{iq} is the coupling strength of the transition. $\mathcal{E}_{\parallel}$ denotes the tangential total electric field to the TMD heterobilayer. The evolution of the surface carrier densities, $N_i(\mathbf{r}, t)$, in each level $i = \{1, 2, 3\}$ of the gain medium is given by typical semiclassical carrier rate equations reading[24,31]

$$\frac{\partial N_3}{\partial t} = \frac{1}{\hbar\omega_{31}}\mathcal{E}_{\parallel}\cdot\frac{\partial \mathcal{P}_s^{(p)}}{\partial t} - \frac{N_3}{\tau_{32}} \tag{2a}$$

$$\frac{\partial N_2}{\partial t} = \frac{1}{\hbar\omega_{21}}\mathcal{E}_{\parallel}\cdot\frac{\partial \mathcal{P}_s^{(m)}}{\partial t} + \frac{N_3}{\tau_{32}} - \frac{N_2}{\tau_{21}} \tag{2b}$$

$$\frac{\partial N_1}{\partial t} = -\frac{1}{\hbar\omega_{31}}\mathcal{E}_{\parallel}\cdot\frac{\partial \mathcal{P}_s^{(p)}}{\partial t} - \frac{1}{\hbar\omega_{21}}\mathcal{E}_{\parallel}\cdot\frac{\partial \mathcal{P}_s^{(m)}}{\partial t} + \frac{N_2}{\tau_{21}} \tag{2c}$$

https://doi.org/10.1021/acsanm.5c04888
ACS Appl. Nano Mater. 2026, 9, 2301−2308

while the total carrier density is conserved, i.e., $N_1 + N_2 + N_3 \equiv N_{tot}$ = const. The parameters for MoS_2/WSe_2 are taken from ref 24 and are typical for the examined TMD heterobilayer.[18−20,22] More specifically, λ_{21} = 1128 nm, λ_{31} = 740 nm, Γ_{21} = 20 Trad/s, Γ_{31} = 70 Trad/s, $\sigma_{21} = 1.43 \times 10^{-8}$ C^2/kg, $\sigma_{31} = 5.32 \times 10^{-7}$ C^2/kg, τ_{21} = 2.5 ns, τ_{32} = 100 fs, and $N_{tot} = 10^{13}$ cm^{-2}. Note that recent studies have shown that λ_{21} (the central wavelength of the interlayer excitonic transition in MoS_2/WSe_2) depends on the twist angle of the two constituent monolayers and for a perfectly aligned bilayer (twist angle ≈ 0°) λ_{21} is closer to 1300 nm.[21] The adopted value of λ_{21} = 1128 nm corresponds to a small misalignment of a few degrees. In addition, a separate surface electric polarization field $\mathcal{P}_s^{(bg)}(\mathbf{r}, t)$ is used to describe the background (nonresonant) dispersive dielectric properties of MoS_2/WSe_2. It follows a typical single-pole Drude−Lorentz relation[32]

$$\frac{\partial^2 \mathcal{P}_s^{(bg)}}{\partial t^2} + \omega_{bg,0}^2 \mathcal{P}_s^{(bg)} = \varepsilon_0 d_{TMD} \omega_{bg,p}^2 \mathcal{E}_{\parallel} \tag{3}$$

where $\omega_{bg,0} = 1.43 \times 10^{16}$ rad/s and $\omega_{bg,p} = 5.99 \times 10^{16}$ rad/s are the background resonance and plasma frequencies fitted to the experimental data of refs 33,34 [see also SI, Section S2 for more details], while $d_{TMD} \approx 1.4$ nm is the thickness of the TMD bilayer.

Equations 1−3 have to be solved in conjunction with Maxwell's equations to assess the response of the proposed MS laser. This task involves a heavy computational burden. Thus, we resort to a much more efficient, yet rigorous and very accurate, approach based on temporal CMT that was very recently developed and demonstrated in ref 27. It has been built upon the aforementioned semiclassical light−matter interactions using first-order perturbation theory and a limited number of approximations widely used in lasing theory. In the context of CMT, the cavity is treated as being lumped, thus the spatial dimension is removed and the response can be obtained by a set of coupled first-order ordinary differential equations (ODEs).[28] Importantly, the coefficients of the CMT equations derived directly from the physical system and are evaluated once through linear eigenvalue simulations of the unit cell of the MS. The ODE for the cavity amplitude of the lasing mode $a(t)$, normalized so that $|a(t)|^2$ is equal to the modal energy per unit length of the SRN stripes, reads[27]

$$\frac{da}{dt} = -j(\omega_{ref} - \omega_{c,0})a - \frac{1}{\tau_{rad}}a - \xi_g\left[j\omega_{ref}p + \frac{dp}{dt}\right] \tag{4}$$

where $\omega_{c,0}$ is the resonance frequency of MD_z in the passive (cold) MS and ω_{ref} is an arbitrarily chosen reference frequency that is used in place of the a priori *unknown* lasing frequency, ω_L. Importantly, the actual lasing frequency is left undetermined and can be evaluated either through a Fourier transform of $a(t)$ in a postprocessing step or through a closed-form relation presented in ref 27. In addition, τ_{rad} is the radiative cavity lifetime related to the respective quality factor through $Q_{rad} = \omega_{c,0}\tau_{rad}/2$, and ξ_g is an overlap factor expressing the strength of interaction between the lasing mode and the sheet gain medium. Eq 4 is complemented by the corresponding ODEs for the polarization amplitude $p(t)$ of the lasing transition and the spatially averaged carrier rate equations. The full system of CMT equations and more details regarding the evaluation of the electromagnetic parameters that feed the CMT framework are presented in SI, Section S3. In order to validate the employed CMT framework, we also conduct nonlinear TD-FEM simulations after appropriately implementing the semiclassical description of light−matter interactions [eqs 1−3 together with Maxwell's equations] in COMSOL Multiphysics (see SI, Section S4 for more details).

We initially set the defect size to d = 20 nm for which we have $\lambda_{c,0}$ = 1127.76 nm ≈ λ_{21} and Q_{rad} = 17,633. The MS laser is then pumped by a normally incident plane wave with pump power density I_p at the pump wavelength of $\lambda_p = \lambda_{31}$ = 740 nm and emits vertically in both ± $\hat{\mathbf{z}}$ directions with a total power density I_{out} at the lasing wavelength λ_L; the upward (downward) output power density in air (substrate) is denoted as $I_{out}^{up}(I_{out}^{dwn})$. The light−light curve (I_{out} vs I_p) evaluated through both CMT (solid line) and TD-FEM (circular markers) is depicted in Figure 3a. A broad range of pump

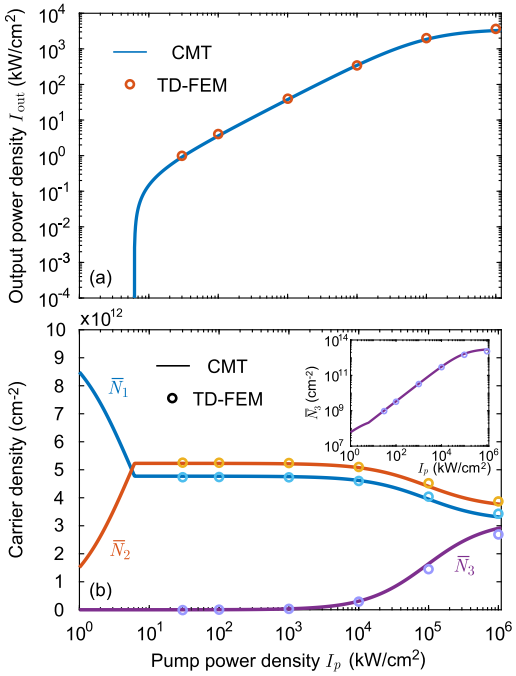

Figure 3. (a) Total emitted power density I_{out}, and (b) spatially averaged surface carrier densities $\bar{N}_i$ in the three levels of the gain medium as a function of the pump power density I_p, obtained by both CMT (solid lines) and TD-FEM (circular markers). Inset in (b) carrier density $\bar{N}_3$ vs I_p in logarithmic scale.

power density levels is covered (1 kW/cm² to 1 GW/cm²) and the agreement between the two methods is excellent. Note that in CMT the total output power density is calculated through $I_{out} = (2/\tau_{rad})|a|^2/\Lambda$. In TD-FEM, on the other hand, I_{out} is assessed by recording the electric field at an appropriate fictitious plane above/below the MS unit cell, followed by a postprocessing Fourier transform to separate the reflected/transmitted pump wave from the emitted wave in the respective direction (inset of Figure 4a).

The examined MS laser exhibits a very low lasing threshold of $I_{p,th}$ = 6.16 kW/cm² and a total efficiency (I_{out}/I_p) of ∼3.7%. This is due to the efficient coupling between the interlayer excitons of MoS_2/WSe_2 and the magnetic dipole qBIC mode of the MS, as well as the enhanced absorption of the pump light by the intralayer excitons of the WSe_2 constituent monolayer. Although the incident pump wave is not coupled to a high-quality-factor mode of the MS, the absorption efficiency, η_p, is still significant with η_p = 9.56%. The power emitted in air (upward emission) is 42.3% of the total emitted power, while

https://doi.org/10.1021/acsanm.5c04888
ACS Appl. Nano Mater. 2026, 9, 2301−2308

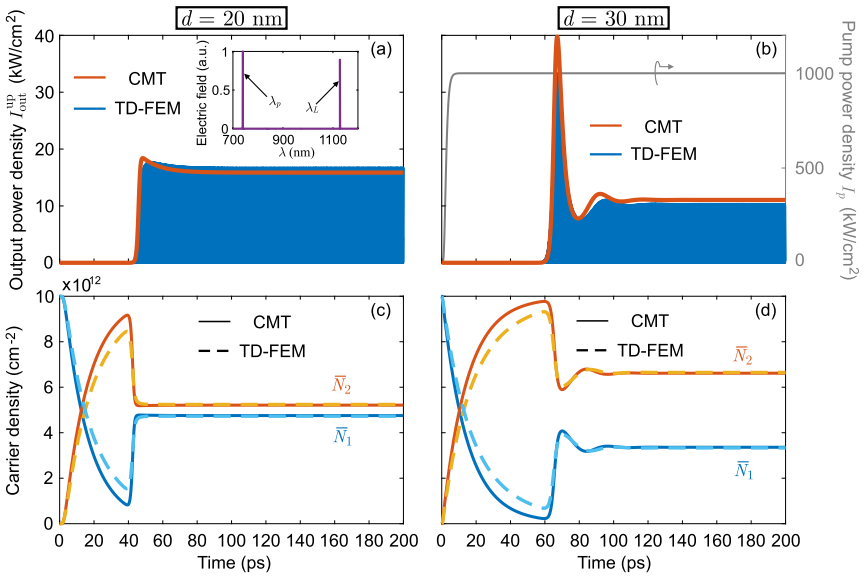

Figure 4. Temporal evolution of (a, b) the output power density in air, I_{out}^{up}, and (c, d) the spatially averaged surface carrier densities $\bar{N}_1$ and $\bar{N}_2$ evaluated through both CMT and TD-FEM. The pump power density is smoothly switched-on until reaching the constant value of I_p = 1 MW/cm^2 [gray curve in (b)]. In (a, c), the defect size is d = 20 nm, while in (b, d) d = 30 nm. Inset in (a) normalized optical spectrum of the electric field in air comprising the reflected pump wave at λ_p and the upward emitted wave at λ_L.

the rest (57.7%) is emitted in the substrate (downward emission), as evaluated either through nonlinear TD-FEM simulations or linear eigenvalue simulations (very good agreement). Note that for a free-standing structure (i.e., absence of substrate), the emitted power would have been equally split in the two $\pm \hat{\mathbf{z}}$ directions, since the lasing mode radiates in the far-field as an in-plane magnetic dipole with no other multipole contributing. In addition, CMT and TD-FEM agree in the prediction of the lasing frequency, for which it holds $\lambda_L \sim \lambda_{21}$ since we had initially aligned the cavity resonance with the peak of the gain spectrum, i.e., $\lambda_{c,0} \approx \lambda_{21}$. We stress that in contrast to other models our CMT framework does not require $\lambda_{c,0} \equiv \lambda_{21}$ and that the detuning between them can be selected freely. The agreement between CMT and TD-FEM is further highlighted in Figure 3b, where the spatially averaged surface carrier densities, $\bar{N}_i$, in the three levels of the gain medium are depicted as a function of I_p.

In Figure 4a, we depict the temporal evolution of the output power density in air, I_{out}^{up}, evaluated through both CMT and TD-FEM, when I_p is smoothly switched-on until reaching the constant value of 1 MW/cm^2 (gray curve in Figure 4b). The corresponding dynamic response of $\bar{N}_1$ and $\bar{N}_2$ is presented in Figure 4c. Once again, the agreement between the two methods is very good both at steady-state and during the transient. The same calculations are also performed for a greater defect size, d = 30 nm, with the corresponding results presented in Figure 4b,d. By increasing the introduced asymmetry, the radiative quality factor decreases to Q_{rad} = 3 250 (cf. Figure 2b). Concurrently, the resonance wavelength is blue-shifted from the central emission wavelength to the value $\lambda_{c,0}$ = 1124.5 nm, thus leading to a suboptimal coupling between the gain medium and the lasing mode. Therefore, the lasing threshold is increased to $I_{p,th}$ = 11.13 kW/cm^2, an almost 2-fold increase compared to d = 20 nm. This is indirectly captured in Figure 4d, where the population inversion at steady state, $\Delta\bar{N}_{21,ss} \propto I_{p,th}$,[27] is much larger than that of Figure 4c. In addition, the output power density at steady-state is now lower for the same level of I_p (cf. Figure 4a, b), while the transient effect is more pronounced with intense relaxation oscillations. The lasing wavelength obtained by TD-FEM simulations is λ_L = 1124.86 nm in this case, in accordance with that estimated through CMT (λ_L = 1124.6 nm).

The importance of the results in Figure 4 should not be overlooked. Using only first-order simplifications and spatial averaging, we were able to reproduce the temporal response of a highly inhomogeneous MS accurately, predicting not only the emitted power but also the carrier densities in the gain medium. CMT can be utilized to probe the underlying physics in complex systems, enables physical interpretations in an efficient manner, and allows for quantitative assessments of the performance.

2.3. Thermal Stability Analysis

In Figure 3a, we examined the CW lasing response of the proposed MS for an extended range of pump power density levels, up to the point where lasing is fully saturated due to the quenching of the intralayer excitonic transition (pump absorption saturation). The latter occurs for I_p > 100 MW/cm^2, i.e., 4 orders of magnitude above the lasing threshold. Nonetheless, in practical nanophotonic lasing structures, the emission process can be hampered at much lower irradiances due to deleterious thermal effects, which can become important in the case of CW pumping (they are typically benign in the case of pulsed pumping). In fact, they are even more pronounced in compact dielectric nanostructures, where the small cavity volume and the absence of metallic interfaces limit the heat removal capabilities.[35] Thus, heat generated by Joule losses remains trapped inside the nanophotonic laser, leading to a substantial increase of the lattice temperature of the gain medium and the subsequent degradation of its luminescence properties.

The heat-removal capability of the examined structure under CW pumping is assessed through heat-transfer simulations with COMSOL Multiphysics. We initially examine a practical realization of the proposed MS laser built on a standard silicon-on-insulator (SOI) wafer (left inset of Figure 5a). The

https://doi.org/10.1021/acsanm.5c04888
ACS Appl. Nano Mater. 2026, 9, 2301−2308

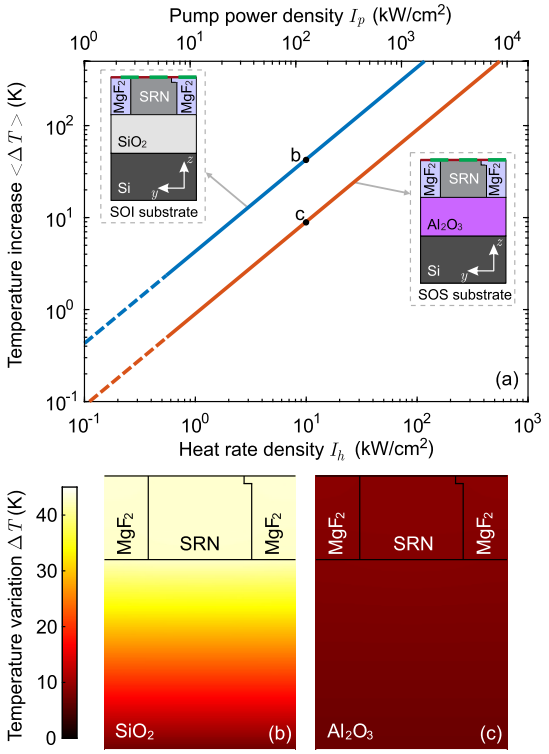

Figure 5. (a) Temperature increase in MoS_2/WSe_2 (spatially averaged) as a function of generated heat rate density I_h for the two different configurations shown in the insets. Dashed lines indicate operation below the lasing threshold. (b, c) Spatial distribution of the temperature variation in the MS unit cell for I_h = 10 kW/cm^2 ($I_p \approx$ 170 kW/cm^2) when the MS resides on top of a (a) standard silicon-on-insulator and (b) silicon-on-sapphire substrate.

thickness of the buried oxide (SiO_2) is 0.5 μm. For the silicon handle layer, a thickness of 10 μm is included in the simulations before being truncated with a constant-temperature boundary condition. As the MS consists of transparent materials at both the pump and lasing wavelengths, the sole heat source is the fraction of the pump power absorbed by the 2D gain medium that is not offered for the amplification of the lasing mode. More specifically, the heat rate density, I_h, is given by $I_h = \eta_p I_p - I_{out}$. We also assume that heat is uniformly generated over the MoS_2/WSe_2 layer. The simulations are conducted with the unit cell of the MS, using continuity boundary conditions at the lateral sides, convective boundary conditions at the interfaces with air [heat-transfer coefficient equal to h = 10 W/(m^{2}K)],[36] and a constant temperature, T_0 = 293 K, boundary condition at the bottom side of Si. The thermal conductivities of the underlying materials are $K_{Si} = K_{SRN}$ = 145 W/(mK), K_{MgF_2} = 28 W/(mK), and K_{SiO_2} = 1.4 W/(mK). In Figure 5a (blue curve), we depict the spatially averaged temperature increase in MoS_2/WSe_2 compared with the ambient temperature T_0 = 293 K, $\langle \Delta T \rangle$, as a function of I_h and I_p. The lasing response is expected to be unobstructed by deleterious thermal effects for almost 2 orders of magnitude above the lasing threshold, where $\langle \Delta T \rangle$ is well below 100 K.

As I_p approaches 1 MW/cm^2, the lattice temperature increases excessively. The low thermal conductivity of the SiO_2 substrate is the main reason for the excessive temperature increase as it restricts the generated heat from being effectively funneled into the high-thermal-conductivity Si layer, where it can be dissipated. This is also evident in Figure 5b, where the spatial variation of the temperature in the yz plane is depicted when I_h = 10 kW/cm^2 ($I_p \approx$ 170 kW/cm^2). A significant improvement of the heat removal capability can be achieved by considering the examined MS laser on top of a silicon-on-sapphire (SOS) wafer (right inset of Figure 5a). Sapphire (Al_2O_3) possesses a thermal conductivity 20 times higher than that of SiO_2 [$K_{Al_2O_3}$ = 28 W/(m K)] and a comparably low refractive index ($n_{Al_2O_3}$ = 1.75). The corresponding spatially averaged temperature increase over MoS_2/WSe_2 is presented in Figure 5a (red curve). The introduction of the high-thermal-conductivity substrate results in a 5-fold reduction of $\langle \Delta T \rangle$ for the same level of I_p (cf. Figure 5b,c), which consequently enables the operation of the MS laser at much higher pump power density levels up to few MW/cm^2 (3 orders of magnitude above threshold).

Note that the presence of the high thermal-conductivity MgF_2 cladding also contributes to heat removal in both of the investigated configurations. This is because the MgF_2 cladding and the SRN core form a uniform high-thermal-conductivity layer across the entire lateral extent of the MS, which effectively drains the generated heat toward the substrate.[27,35]

3. CONCLUSIONS

In summary, we have proposed an MS laser comprising SRN stripes periodically arrayed in a subdiffractive lattice and overlaid with the contemporary MoS_2/WSe_2 TMD heterobilayer. Highly efficient lasing in the NIR is enabled by the enhanced coupling between the qBIC magnetic dipole mode supported by the MS and the long-lived interlayer excitons hosted by the 2D gain medium. The modal properties of the quasi-dark resonance and the physical mechanism behind its transformation from BIC to qBIC are elucidated through eigenfrequency simulations and multipole expansion analysis. The proposed structure is characterized by a very low lasing threshold of only a few kW/cm^2. A comprehensive thermal stability analysis through heat-transfer simulations has shown that the laser can function free from deleterious thermal effect in a wide range of pump power densities (up to 3 orders of magnitude above threshold), where the MS laser can deliver practical levels of output power.

The lasing response of the examined MS was thoroughly assessed through a highly efficient temporal CMT framework verified by full-wave nonlinear TD-FEM simulations. The agreement between the two methods is excellent both at steady state and during the transient. The validation of the CMT framework opens new avenues for efficiently designing and studying elaborate MS laser structures based on 2D or 3D gain media without resorting to time-consuming full-wave nonlinear simulations.[37]

In terms of practicality, the proposed MS can be fabricated by a two-step lithography and etching process. In the first step, the partially etched defect is formed. Subsequently, a second lithography and etching process follows for the fully etched (down to the buried oxide) regions. Fine control over the shallow-etch depth and the alignment between the two lithography steps is required.

■ ASSOCIATED CONTENT

Supporting Information

The Supporting Information is available free of charge at https://pubs.acs.org/doi/10.1021/acsanm.5c04888.

https://doi.org/10.1021/acsanm.5c04888
ACS Appl. Nano Mater. 2026, 9, 2301−2308

Impact of finite MS extent, background dielectric properties of MoS_2/WSe_2, details on the CMT framework including the full system of CMT equations, and details regarding the nonlinear TD-FEM simulations. (PDF)

AUTHOR INFORMATION

Corresponding Authors

Georgios Nousios − *School of Electrical and Computer Engineering, Aristotle University of Thessaloniki (AUTH), Thessaloniki GR-54124, Greece;* orcid.org/0000-0002-7864-5066; Email: gnnousios@ece.auth.gr

Odysseas Tsilipakos − *Theoretical and Physical Chemistry Institute, National Hellenic Research Foundation, Athens GR-11635, Greece;* orcid.org/0000-0003-4770-0955; Email: otsilipakos@eie.gr

Authors

Thomas Christopoulos − *Laboratoire Photonique, Numérique et Nanosciences (LP2N), IOGS-Université de Bordeaux-CNRS, Talence 33400, France;* orcid.org/0000-0003-3536-9564

Emmanouil E. Kriezis − *School of Electrical and Computer Engineering, Aristotle University of Thessaloniki (AUTH), Thessaloniki GR-54124, Greece*

Complete contact information is available at: https://pubs.acs.org/10.1021/acsanm.5c04888

Funding

The open access publishing of this article is financially supported by HEAL-Link.

Notes

The authors declare no competing financial interest.

ACKNOWLEDGMENTS

O.T. acknowledges fruitful discussions with Dr. Thomas Koschny.

REFERENCES

(1) Vaskin, A.; Kolkowski, R.; Koenderink, A. F.; Staude, I. Light-emitting metasurfaces. *Nanophotonics* **2019**, *8*, 1151−1198.

(2) Al-Hamadani, A.; Gupta, V.; Montaño-Priede, J. L.; Thomas, R.; Muravitskaya, A.; Markey, L.; Roux-Byl, C.; Pons, T.; Zapata-Herrera, M.; Zabala, N.; Weeber, J.-C.; Suckow, S.; Vogel, N.; Bouillard, J.-S. G.; Adawi, A. M. Photoluminescence Enhancement at Telecom Wavelengths from PbS/CdS Quantum Dots coupled to a Plasmonic Crescent Metasurface. *ACS Applied Nano Materials* **2025**, *8*, 19474−19482.

(3) Zografopoulos, D. C.; Tsilipakos, O. Recent advances in strongly resonant and gradient all-dielectric metasurfaces. *Materials Advances* **2023**, *4*, 11−34.

(4) Cui, C.; Zhou, C.; Yuan, S.; Qiu, X.; Zhu, L.; Wang, Y.; Li, Y.; Song, J.; Huang, Q.; Wang, Y.; Zeng, C.; Xia, J. Multiple Fano Resonances in Symmetry-Breaking Silicon Metasurface for Manipulating Light Emission. *ACS Photonics* **2018**, *5*, 4074−4080.

(5) Campione, S.; Liu, S.; Basilio, L. I.; Warne, L. K.; Langston, W. L.; Luk, T. S.; Wendt, J. R.; Reno, J. L.; Keeler, G. A.; Brener, I.; Sinclair, M. B. Broken Symmetry Dielectric Resonators for High Quality Factor Fano Metasurfaces. *ACS Photonics* **2016**, *3*, 2362−2367.

(6) Zhang, B.; Dong, A.; Wang, J.; Qin, M.; Liu, J.-q.; Huang, W.; Xiao, S.; Li, H. Strong Coupling and Electromagnetically Induced Transparency in Multiple-BIC-Driven Metasurfaces. *Nano Lett.* **2025**, *25*, 4568−4575.

(7) Qin, M.; Wei, G.; Xu, H.; Ma, R.; Li, H.; Gao, W.; Liu, J.; Wu, F. Polarization-insensitive and polarization-controlled dual-band third-harmonic generation in silicon metasurfaces driven by quasi-bound states in the continuum. *Appl. Phys. Lett.* **2024**, *124*, No. 051703.

(8) Ha, S. T.; Fu, Y. H.; Emani, N. K.; Pan, Z.; Bakker, R. M.; Paniagua-Domínguez, R.; Kuznetsov, A. I. Directional lasing in resonant semiconductor nanoantenna arrays. *Nat. Nanotechnol.* **2018**, *13*, 1042−1047.

(9) Wu, M.; Ha, S. T.; Shendre, S.; Durmusoglu, E. G.; Koh, W. K.; Abujetas, D. R.; Sánchez-Gil, J. A.; Paniagua-Domínguez, R.; Demir, H. V.; Kuznetsov, A. I. Room-Temperature Lasing in Colloidal Nanoplatelets via Mie-Resonant Bound States in the Continuum. *Nano Lett.* **2020**, *20*, 6005−6011.

(10) Cui, C.; Yuan, S.; Qiu, X.; Zhu, L.; Wang, Y.; Li, Y.; Song, J.; Huang, Q.; Zeng, C.; Xia, J. Light emission driven by magnetic and electric toroidal dipole resonances in a silicon metasurface. *Nanoscale* **2019**, *11*, 14446−14454.

(11) Prokhorov, A. V.; Gubin, M. Y.; Shesterikov, A. V.; Arsenin, A. V.; Volkov, V. S.; Evlyukhin, A. B. Lasing Effect in Symmetrical van der Waals Heterostructured Metasurfaces Due to Lattice-Induced Multipole Coupling. *Nano Lett.* **2023**, *23*, 11105−11111.

(12) Yang, J.-H.; Huang, Z.-T.; Maksimov, D. N.; Pankin, P. S.; Timofeev, I. V.; Hong, K.-B.; Li, H.; Chen, J.-W.; Hsu, C.-Y.; Liu, Y.-Y.; Lu, T.-C.; Lin, T.-R.; Yang, C.-S.; Chen, K.-P. Low-Threshold Bound State in the Continuum Lasers in Hybrid Lattice Resonance Metasurfaces. *Laser Photonics Rev.* **2021**, *15*, No. 2100118.

(13) Psilodimitrakopoulos, S.; Mouchliadis, L.; Paradisanos, I.; Lemonis, A.; Kioseoglou, G.; Stratakis, E. Ultrahigh-resolution nonlinear optical imaging of the armchair orientation in 2D transition metal dichalcogenides. *Light: Science & Applications* **2018**, *7*, 18005−18005.

(14) Wang, J.; Xu, H.; Si, J.; Wu, H.; Wang, H.; Qiu, H.; Jiang, H.; Qin, M.; Liu, J.-Q.; Wu, F.; Li, H. Chirality inversion for tailoring light generation in nonlinear van der Waals metasurfaces. *Appl. Phys. Lett.* **2025**, *127*, No. 061701.

(15) Elbanna, A.; Jiang, H.; Fu, Q.; Zhu, J.-F.; Liu, Y.; Zhao, M.; Liu, D.; Lai, S.; Chua, X. W.; Pan, J.; Shen, Z. X.; Wu, L.; Liu, Z.; Qiu, C.-W.; Teng, J. 2D Material Infrared Photonics and Plasmonics. *ACS Nano* **2023**, *17*, 4134−4179.

(16) Cadore, A. R.; et al. Monolayer WS_2 electro- and photoluminescence enhancement by TFSI treatment. *2D Materials* **2024**, *11*, No. 025017.

(17) Barth, I.; Deckart, M.; Conteduca, D.; Arruda, G. S.; Hayran, Z.; Pasko, S.; Krotkus, S.; Heuken, M.; Monticone, F.; Krauss, T. F.; Martins, E. R.; Wang, Y. Lasing from a Large-Area 2D Material Enabled by a Dual-Resonance Metasurface. *ACS Nano* **2024**, *18*, 12897−12904.

(18) Jiang, Y.; Chen, S.; Zheng, W.; Zheng, B.; Pan, A. Interlayer exciton formation, relaxation, and transport in TMD van der Waals heterostructures. *Light Sci. Appl.* **2021**, *10*, 72.

(19) Palummo, M.; Bernardi, M.; Grossman, J. C. Exciton Radiative Lifetimes in Two-Dimensional Transition Metal Dichalcogenides. *Nano Lett.* **2015**, *15*, 2794−2800.

(20) Selig, M.; Berghäuser, G.; Richter, M.; Bratschitsch, R.; Knorr, A.; Malic, E. Dark and bright exciton formation, thermalization, and photoluminescence in monolayer transition metal dichalcogenides. *2D Materials* **2018**, *5*, No. 035017.

(21) Lin, Q.; Fang, H.; Kalaboukhov, A.; Liu, Y.; Zhang, Y.; Fischer, M.; Li, J.; Hagel, J.; Brem, S.; Malic, E.; Stenger, N.; Sun, Z.; Wubs, M.; Xiao, S. Moiré-engineered light-matter interactions in MoS_2/WSe_2 heterobilayers at room temperature. *Nat. Commun.* **2024**, *15*, 8762.

(22) Liu, Y.; Fang, H.; Rasmita, A.; Zhou, Y.; Li, J.; Yu, T.; Xiong, Q.; Zheludev, N.; Liu, J.; Gao, W. Room temperature nanocavity laser with interlayer excitons in 2D heterostructures. *Sci. Adv.* **2019**, *5*, No. eaav4506.

(23) Huang, X.; Fang, H.; Kadkhodazadeh, S.; Nielsen, M. R.; Lin, Q.; Sun, Z.; Wubs, M.; Xiao, S. *On-chip integrated light sources with MoS2/WSe2 moiré superlattices at telecom wavelengths* **2025**, *25*, 1234.
(24) Nousios, G.; Christopoulos, T.; Tsilipakos, O.; Kriezis, E. E. Theoretical Analysis of Integrated Nanophotonic Q-Switched Laser Based on Gain and Saturable Absorption by Two-Dimensional Materials. *Adv. Photonics Res.* **2024**, *5*, No. 2300249.
(25) Murai, S.; Abujetas, D. R.; Castellanos, G. W.; Sánchez-Gil, J. A.; Zhang, F.; Rivas, J. G. Bound States in the Continuum in the Visible Emerging from out-of-Plane Magnetic Dipoles. *ACS Photonics* **2020**, *7*, 2204−2210.
(26) Savinov, V.; Fedotov, V. A.; Zheludev, N. I. Toroidal dipolar excitation and macroscopic electromagnetic properties of metamaterials. *Phys. Rev. B* **2014**, *89*, No. 205112.
(27) Nousios, G.; Christopoulos, T.; Tsilipakos, O.; Kriezis, E. E. Integrated Lasers with Transition-Metal-Dichalcogenide Heterostructures: Analysis and Design Utilizing Coupled-Mode Theory for Two-Dimensional Materials. *Phys. Rev. Appl.* **2023**, *19*, No. 064027.
(28) Christopoulos, T.; Tsilipakos, O.; Kriezis, E. E. Temporal coupled-mode theory in nonlinear resonant photonics: From basic principles to contemporary systems with 2D materials, dispersion, loss, and gain. *J. Appl. Phys.* **2024**, *136*, No. 011101.
(29) Wang, T.; Ng, D. K. T.; Ng, S.-K.; Toh, Y.-T.; Chee, A. K. L.; Chen, G. F. R.; Wang, Q.; Tan, D. T. H. Supercontinuum generation in bandgap engineered, back-end CMOS compatible silicon rich nitride waveguides. *Laser & Photonics Reviews* **2015**, *9*, 498−506.
(30) Nousios, G.; Algorri, J.; Fuscaldo, W.; Dell'Olio, F.; Romano, S.; Zito, G.; Miranda, B.; Ding, Y.; Dmitriev, V.; Andreani, L.; Galli, M.; Tsilipakos, O.; Kriezis, E.; Zografopoulos, D. Silicon slot metasurface supporting a multitude of bound states in the continuum: theoretical and experimental studies. *Optics & Laser Technology* **2025**, *192*, No. 113398.
(31) Fietz, C.; Soukoulis, C. M. Finite element simulation of microphotonic lasing system. *Opt. Express* **2012**, *20*, 11548−11560.
(32) Christopoulos, T.; Nousios, G.; Kriezis, E. E.; Tsilipakos, O. Quasinormal mode theory for multiresonant metasurfaces with superwavelength periodicity involving two-dimensional materials. *Phys. Rev. B* **2024**, *110*, No. 245407.
(33) Liu, H.-L.; Shen, C.-C.; Su, S.-H.; Hsu, C.-L.; Li, M.-Y.; Li, L.-J. Optical properties of monolayer transition metal dichalcogenides probed by spectroscopic ellipsometry. *Appl. Phys. Lett.* **2014**, *105*, 201905.
(34) Hsu, C.; Frisenda, R.; Schmidt, R.; Arora, A.; de Vasconcellos, S. M.; Bratschitsch, R.; van der Zant, H. S. J.; Castellanos-Gomez, A. Thickness-Dependent Refractive Index of 1L, 2L, and 3L MoS_2, $MoSe_2$, WS_2, and WSe_2. *Adv. Opt. Mater.* **2019**, *7*, No. 1900239.
(35) Wen, P.; Tiwari, P.; Scherrer, M.; Lörtscher, E.; Gotsmann, B.; Moselund, K. E. Thermal Simulation and Experimental Analysis of Optically Pumped InP-on-Si Micro- and Nanocavity Lasers. *ACS Photonics* **2022**, *9*, 1338−1348.
(36) Tsilipakos, O.; Yioultsis, T. V.; Kriezis, E. E. Theoretical analysis of thermally tunable microring resonator filters made of dielectric-loaded plasmonic waveguides. *J. Appl. Phys.* **2009**, *106*, No. 093109.
(37) Christopoulos, T.; Hizanidis, J.; Nousios, G.; Kriezis, E. E.; Tsilipakos, O. Assessing two-dimensional materials as enablers for passively *Q*-switched nanophotonic lasers. *Phys. Rev. Appl.* **2025**, *24*, No. 014028.

https://doi.org/10.1021/acsanm.5c04888
ACS Appl. Nano Mater. 2026, 9, 2301−2308